ARTICLE OPEN

Check for updates

Hole-type superconducting gatemon qubit based on Ge/Si core/shell nanowires

Enna Zhuo[1,2,7], Zhaozheng Lyu[1,3,7✉], Xiaopei Sun[1,2,7], Ang Li[4,7], Bing Li[1,2], Zhongqing Ji[1], Jie Fan[1], E.P.A.M. Bakkers[5], Xiaodong Han[4], Xiaohui Song[1,2,6], Fanming Qu[1,2,3,6], Guangtong Liu[1,2,3,6], Jie Shen[1,2,6] and Li Lu[1,2,3,6✉]

We demonstrate that superconducting gatemon qubits based on superconductor-semiconductor-superconductor Josephson junctions can be constructed on hole-type Ge/Si core/shell nanowires. The frequency of the qubit can be set firstly by controlling the diffusion of Al in the nanowire via thermal annealing, which yields a suitable critical supercurrent allowing the qubit frequency to be within the experimentally accessible range, and then by fine tuning of a gate voltage, by which an accurate adjustment of the frequency can be realized. On the resulted qubit, Rabi oscillation with an energy relaxation time $T_1 \sim 180$ ns was observed in the time domain, an average decoherence time $T_2^* \sim 15$ ns was obtained, and the gate voltage dependence of both T_1 and T_2^* was investigated. Such a hole-type superconducting gatemon qubit, based on materials with strong spin-orbit coupling and potentially the absence of hyperfine interaction after isotope purification, could be used for exploring the quantum coherence phenomena of hole-gas and even Majorana physics in Ge-based quantum devices.

npj Quantum Information (2023)9:51 ; https://doi.org/10.1038/s41534-023-00721-9

INTRODUCTION

The future architecture for quantum computation should integrate and take the advantages of different types of quantum circuits[1], such as spin qubits with small footprints[2–4], superconducting qubits capable for high-fidelity readout and control[5,6], and topological qubits supposedly immune from environmental noise[7]. Germanium-based materials hold excellent prospects for constructing such hybrid architecture, for that the states of the valence bands in these materials are featured with high hole mobilities[8,9], large and tunable spin-orbit coupling[10,11], and weak hyperfine interaction[12]. So far, Ge-based spin qubits have already been realized in planar heterostructures[13–15], Ge hut wires[16,17], and Ge/Si core/shell nanowires[18–20]. But Ge-based superconducting qubits are yet to be realized.

For constructing Ge-based superconducting qubits, one needs high-quality Josephson junctions (JJs) on Ge-based materials. Along this direction, proximity-induced superconductivity in Ge was first realized in a Josephson field-effect transistor (JoFET) based on a Ge/Si core/shell nanowire[21]. Later on, with the application of an annealing process in Al-Ge systems[22], clean and atomically sharp Al-Ge interfaces were further realized in the core/shell nanowire systems, and JJs with controllable critical supercurrent were obtained[23–25]. Besides Ge/Si nanowires, proximity-induced superconductivities were also demonstrated in undoped Ge/SiGe heterostructures by contacting the material with Al, Al/Nb, or PtSiGe electrodes[26–28] to form hybrid devices such as JoFETs, superconducting quantum dots and superconducting quantum interference devices[29,30].

Based on the annealing technique mentioned above, in this work we were able to experimentally embed a Ge/Si core/shell nanowire, in which the hole mobility is around 2000 $cm^2 V^{-1} s^{-1}$ at 4 K[31], into a superconducting transmon qubit. The JJ with highly transparent interfaces between the superconducting electrodes and the 1D hole gas, and also with a desired critical supercurrent, was obtained by carefully controlling the diffusion of Al in Ge/Si nanowire via thermal annealing. In the resulted device, hereafter referred to as a gatemon[32], we demonstrated the electrical control of the qubit frequency over a wide frequency range and the coherent manipulation of the qubit states. Although currently the coherence time of our gatemon is short compared to other types of qubits, probably because gatemons are relatively susceptible to charge noise, the coherence time can be improved by optimizing the material quality and the device fabrication procedures.

RESULTS

Experimental set-up and measurement configuration

Shown in Fig. 1a is the optical micrograph of the gatemon device. The coplanar waveguide resonator, the shunt capacitance C_q in the qubit, and the coupling capacitance C_g between the qubit and the resonator were all patterned by wet etched Al film on the sapphire substrate [Fig. 1a]. For the nonlinear inductance part of the qubit, by applying a nanowire transfer technique based on tip and vitrified poly propylene carbonate (PPC), a Ge/Si nanowire was precisely transferred onto the place where a bottom gate electrode with an insulating cap was pre-fabricated. The insulating layer was 35 nm thick HfO_2 film grown by atomic layer deposition. Then, Al electrodes were deposited on the nanowire to form the Al-Ge/Si nanowire-Al JJ. In order to obtain a suitable Josephson energy E_J, we developed a method to monitor the resistance of the JJ during vacuum thermal annealing in a probe station, letting Al and Ge to inter-diffuse until the resistance of JJ drops to $\sim$ 2.9 kΩ at room temperature. This junction resistance corresponds to a Josephson energy $E_J/h \sim 15$ GHz at $\sim$ 10 mK, as presumed

[1]Beijing National Laboratory for Condensed Matter Physics, Institute of Physics, Chinese Academy of Sciences, Beijing 100190, China. [2]School of Physical Sciences, University of Chinese Academy of Sciences, Beijing 100049, China. [3]Hefei National Laboratory, Hefei 230088, China. [4]Beijing Key Laboratory of Microstructure and Property of Advanced Materials, Beijing University of Technology, Beijing 100124, China. [5]Department of Applied Physics, Eindhoven University of Technology, 5600 MB Eindhoven, The Netherlands. [6]Songshan Lake Materials Laboratory, Dongguan, Guangdong 523808, China. [7]These authors contributed equally: Enna Zhuo, Zhaozheng Lyu, Xiaopei Sun, Ang Li. ✉email: lyuzhzh@iphy.ac.cn; lilu@aphy.iphy.ac.cn

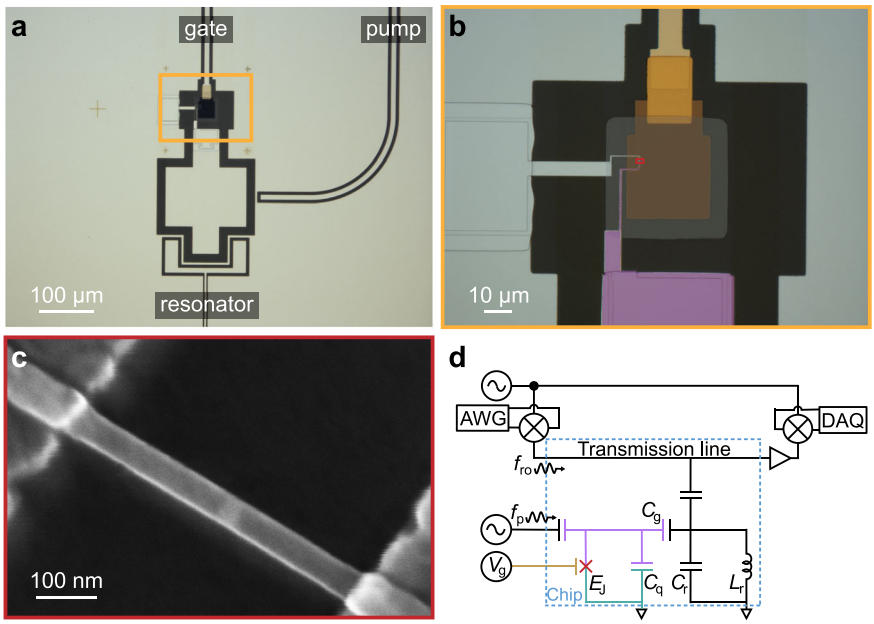

Fig. 1 Ge/Si nanowire-based superconducting gatemon qubit. a Optical micrograph of the gatemon device. The gate-tunable qubit is capacitively coupled to the resonator and the pump line. **b** False-color optical micrograph of the qubit [orange rectangle in (**a**). The bottom gate consists of the 3/10/3 nm thick Ti/Au/Ti bottom electrode (brown) and 35 nm thick HfO_2 insulating layer (gray). The JJ is shunted by the capacitance of the island (purple) to the surrounding ground plane (cyan). **c** Scanning electron micrograph of the Ge/Si-Al JJ [red rectangle in (**b**). A junction with two clear interfaces separated by ~ 30 nm was formed by diffusion of Al during annealing. **d** Schematic of the readout and control circuit, including instruments: signal generator, arbitrary waveform generator (AWG), IQ mixers (⊗), cryogenic HEMT amplifier, data acquisition (DAQ) card. There is a total of −110 dB attenuation from the signal generator to the chip. C_r and L_r are the effective capacitance and inductance of the resonator, respectively.

from the dc transport measurements on the same batch of nanowires (see Supplementary Note 1). The junction region on the nanowire, ~ 30 nm in length and with a light-gray color in the scanning electron micrograph, can be clearly seen in Fig. 1c. The device was measured by using standard circuit quantum electrodynamics (cQED) techniques in a dilution refrigerator down to a temperature as low as ~ 10 mK. In the cQED system, the qubit (artificial atom) is coupled to the microwave resonator via the Jaynes-Cummings-type interaction, which enables the quantum nondemolition measurement of the qubit state in the dispersive limit.

Spectroscopy and the qubit-resonator coupling strength

We firstly measured the response of the resonator spectrum with the gate voltage V_g in the dispersive regime ($|\triangle| \gg g$), by applying a low-power readout microwave signal f_{ro} in the transmission line [Fig. 2a], where $\triangle$ is the qubit-resonator detuning and g is the strength of the qubit-resonator coupling. As the qubit is in the ground state, the resonance frequency of the resonator is shifted from the bare resonance frequency ($f_r = 6.85$ GHz) by Lamb shift ($-g^2/\triangle$), which causes the resonator frequency to respond with the gate voltage that adjusts the qubit frequency f_q.

The readout of the qubit is achieved by measuring the qubit-state-dependent resonator response with the cQED approach, with an additional pump microwave pulse f_p applied to perform the state transitions of the qubit. Figure 2b shows the measured qubit spectrum as a function of f_p and V_g. Since our device is operated in the transmon regime[33], $E_J \gg E_c$, where $E_c = e^2/2C_\Sigma$ is the charging energy of the qubit and $E_J = I_C\Phi_0/2\pi$ is the Josephson energy of the qubit, the transition frequency between the lowest two qubit levels is generally given by $f_q = \sqrt{8E_JE_C}/h - E_C/h$, and the anharmonicity of the qubit corresponds to the charging energy, $\eta = -E_c$.

In the qubit spectrum, two resonant frequencies can be distinguished, as shown in the inset of Fig. 2b. The higher resonant frequency f_q corresponds to the single-photon transition between the $|0\rangle$ and $|1\rangle$ states of the qubit, and the lower frequency $f_{02}/2$ corresponds to the double-photon transition between the $|0\rangle$ and $|2\rangle$ states of the qubit. From the anharmonicity $\eta/h = 2f_q - f_{02}$, the charging energy $E_c/h =$ 218 MHz (a total capacitance $C_\Sigma \approx 88.9$ fF) can be calculated. The qubit frequency f_q exhibits a tunable range from 3.6 GHz to 6.0 GHz by sweeping the gate voltage, since the gate voltage changes the hole density in the nanowire, hence changing the critical supercurrent I_C and the Josephson energy E_J of the JJ. With the charging energy derived previously, I_C of the JJ in the qubit is estimated to be 17 ~ 45 nA, which is consistent with our results obtained in dc transport measurements (see Supplementary Note 1). And it is found that when the detuning $|\triangle|$ is reduced by tuning the gate voltage, the spectrum broadens so that the two resonance peaks can no longer be distinguished.

In addition, two phenomena can be observed in the qubit spectrum. Firstly, the resonance peaks in the resonator spectrum and qubit spectrum have repeatable synchronous jumps at certain gate voltages, presumably due to the jumps of trapped charges in the insulating layer of the bottom gate. The instability of the trapped charges can also create charge noise, causing fluctuations in the qubit energy levels, broadening of the qubit spectrum, and reducing the coherence time. Secondly, there are level anti-crossings in the qubit spectrum at $f_p = 4.6$, 4.9, 5.3, 5.7 GHz due to the couplings between the qubit and some microscopic two-level systems (TLSs)[34] that are not tuned by V_g. The splitting is positively correlated with the strength of qubit-TLSs coupling. More data from similar devices we measured show that by reducing the length of the junction region where the electric field of the plasma mode of the qubit is the strongest[35], we can effectively reduce the number of strongly coupled TLSs. It indicates that these TLSs may mainly originate from the defects in the oxide layer on the surface of the nanowire and/or in the insulating layer HfO_2 of the bottom gate.

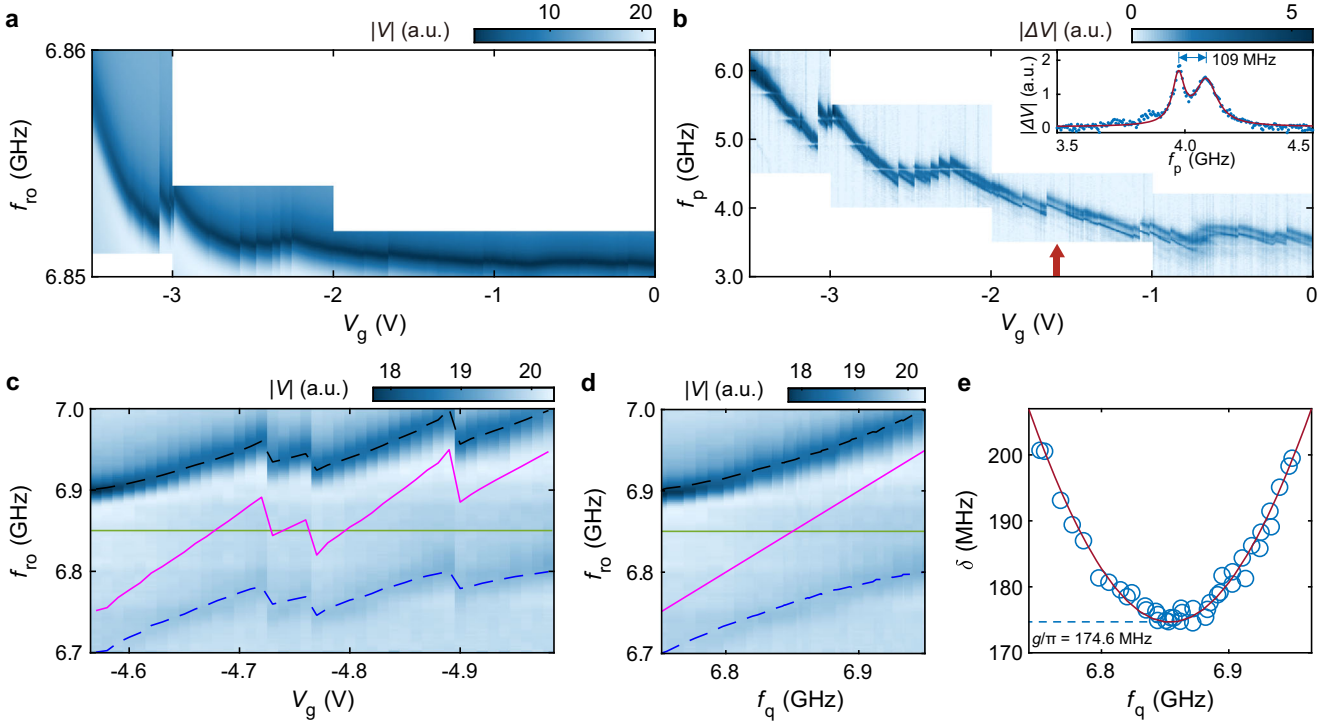

Fig. 2 Spectroscopy of a Ge/Si nanowire-based gatemon qubit. a Resonator spectrum as a function of the readout frequency f_{ro} and the gate voltage V_g in the dispersive regime ($|\triangle| \gg g$), measured with the readout power $P_{ro} = 0.1$ mW at the generator of the readout microwave signal. **b** Qubit spectrum as a function of the pump frequency f_p and V_g in the dispersive regime. The pump-generator power is set to $P_p = 0.3$ mW and the resonator is probed on-resonance with $P_{ro} = 0.1$ mW. Inset: A two-peaks Lorentzian (solid line) with the peak difference $\eta/2h = 109$ MHz fitted to a line-cut in (**b**) at $V_g = -1.59$ V (pointed by the red arrow). **c** Resonator spectrum as a function of f_{ro} and V_g in the strong-coupling regime ($f_q \sim f_r$) with $P_{ro} = 0.1$ mW. The black and blue dashed line indicate two local minima of the hybrid state frequencies $f_\pm$ in the spectrum, and the solid pink line indicates the gate-voltage dependent qubit frequency $f_q(V_g)$ extracted from the data. The bare resonator frequency $f_r = 6.85$ GHz is marked by the solid green line. **d** Resonator spectrum re-plotted as a function of f_{ro} and f_q of the data from (**c**). **e** Frequency splitting δ between the hybridized qubit-resonator states, extracted from (**c**), as a function of f_q. From the fit shown with the solid curve, the qubit-resonator coupling strength $g/2\pi = 87$ MHz is extracted.

In order to investigate the qubit-resonator coupling strength g, the resonator spectrum was measured as a function of f_{ro} and V_g in the strong-coupling regime ($f_q \sim f_r$) [Fig. 2c]. The splitting of the resonance frequency of the resonator, known as vacuum Rabi splitting, was observed which indicates hybridization between the resonator and the qubit states. The frequencies of the hybrid states, written as $f_\pm = \left[f_q + f_r \pm \sqrt{(f_q - f_r)^2 + 4(g/2\pi)^2}\right]/2$, are extracted from Fig. 2c to obtain the qubit frequency $f_q = f_+ + f_- - f_r$ and the splitting $\delta = f_+ - f_-$. The data in Fig. 2c are replotted as a function of the qubit frequency f_q, as shown in Fig. 2d, which presents anti-crossing of the hybrid states more clearly. According to the formula $\delta = \sqrt{(f_q - f_r)^2 + 4(g/2\pi)^2}$, the coupling strength between the qubit and the resonator, $g/2\pi = 87$ MHz, is obtained by fitting the splitting δ as a function of f_q [Fig. 2e], and then the coupling capacitance $C_g = 4.6$ fF can be calculated, which is consistent with the simulation for the circuit. This coupling strength g is suitable for allowing a wide frequency range for dispersive readout and yet maintaining the vacuum Rabi splitting to be resolved.

Rabi oscillations and coherence times

Next, we demonstrated the coherent quantum manipulation of the qubit in the time domain. Since in our device the resonator transient response time (about 300 ns, see Supplementary Note 2) is greater than the energy relaxation time of the qubit ($T_1 \sim 100$ ns), it is impossible to read out the qubit after coherent manipulation with two tones measurement in time domain. Therefore, we used the method of weak continuous measurement[36] to study our device. As shown in the microwave pulse sequence in the upper panel of Fig. 3a, in the case of continuous input of f_{ro}, the qubit is pumped and read out after the number of photons in the resonator is stable.

While varying the pump pulse duration τ_{Rabi}, the Rabi oscillation of the qubit as a function of the pump frequency f_p was measured at $f_q = 6.07$ GHz ($V_g = -3.5$ V) [Fig. 3a]. Figure 3b shows the Rabi oscillations for different powers of the pump microwave pulse at $f_q = 6.07$ GHz. By fitting to the data, the frequency of the Rabi oscillation f_{Rabi} is extracted, which is proportional to $\sqrt{P_p}$, as shown in Fig. 3c, indicating that the states of the qubit based on Ge/Si nanowire are coherent. In addition to the one centered at 6.07 GHz, there is another series of Rabi oscillations centered at 5.91 GHz, as shown in Fig. 3a. We attribute it to double-photon transitions between $|0\rangle$ and $|2\rangle$ states.

In order to further obtain the energy relaxation time T_1 of the qubit, we applied a microwave pulse R_π (calibrated from the Rabi oscillation) to excite the qubit to state $|1\rangle$, and detected the qubit state after various delay time τ. It yielded an exponentially decaying trace, with a relaxation time $T_1 = 112.2 \pm 4.3$ ns.

To further investigate the decoherence time of the qubit, we measured the response of the qubit spectrum at different pump power P_p. As shown in Fig. 3e, when P_p is low, only the first spectroscopic line representing the single-photon transition between $|0\rangle$ and $|1\rangle$ states is detected. With the increase of P_p, the mode of double-photon transition between $|0\rangle$ and $|2\rangle$ states appears. The half width at half maximum (HWHM) of the spectroscopic line depends on the pump power and qubit decoherence,

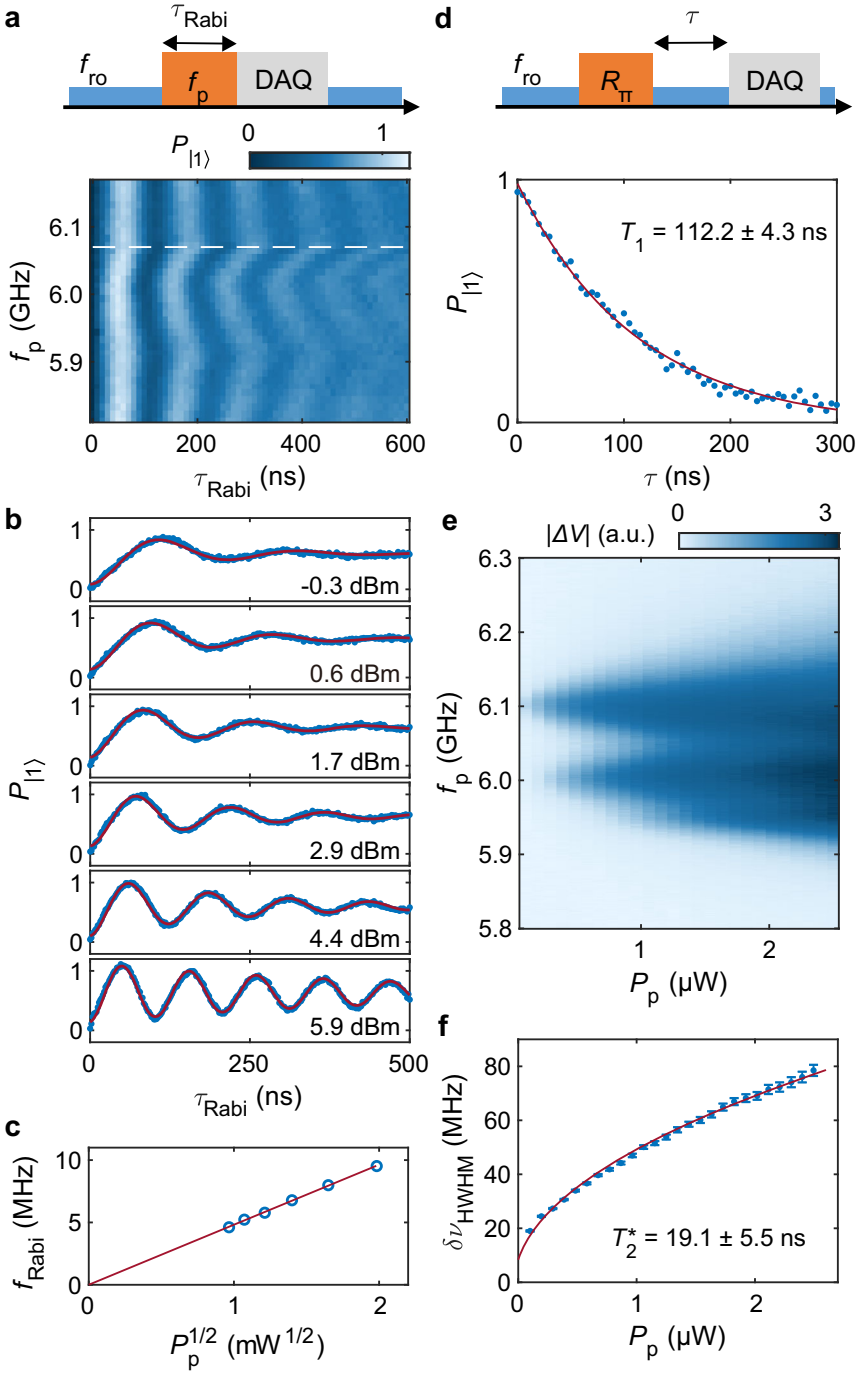

Fig. 3 Quantum coherence of a Ge/Si nanowire-based qubit. a Coherent Rabi oscillations as a function of the pump frequency f_p performed at $V_g = -3.5$ V by applying the microwave pulse sequence shown in the upper panel. The measurement settings are the pump power $P_p = 4.4$ dBm and the readout power $P_{ro} = 0.01$ mW. The dash line is plotted at $f_p = 6.07$ GHz. **b** Coherent qubit oscillations at the qubit resonant frequency $f_q = 6.07$ GHz measured with different pump powers P_p at $V_g = -3.5$ V. The solid curves are fits to exponentially damped sine functions. **c** The Rabi frequency f_{Rabi}, obtained from the fits in (**b**), as a function of $\sqrt{P_p}$ with a fit to the expected linear dependence. **d** Energy relaxation time T_1 measurement performed at $f_q = 6.07$ GHz ($V_g = -3.5$ V) using a π-pulse R_π calibrated from the Rabi oscillation at $P_p = 4.4$ dBm. The fit to an exponential decay yields $T_1 = 112.2 \pm 4.3$ ns. **e** Qubit spectrum as a function of the pump frequency f_p and the pump power P_p at $V_g = -3.5$ V. The resonator is probed on-resonance with $P_{ro} = 0.1$ mW. **f** Dependence of the half width at half maximum $\delta\nu_{HWHM}$ on the pump power P_p, where $\delta\nu_{HWHM}$ of the spectroscopic line is extracted from the Lorentzian fitting to the data in (**e**). Error bars represent the standard deviation. The solid line is a best fit, yielding the inhomogeneous dephasing time $T_2^* = 19.1 \pm 5.5$ ns.

$2\pi\delta\nu_{HWHM} = 1/T_2^* = \left(1/T_2^2 + n\omega_{vac}^2 T_1/T_2\right)^{1/2}$ [37,38], where $\omega_{vac} = 2g$ is the vacuum Rabi frequency, n is the average number of photons in the resonator, and the pump power P_p is proportional to n. The decoherence rate γ_2 corresponds to $2\pi\delta\nu_{HWHM}$ in the low power limit ($P_p \propto n \to 0$). Fitting the data of the first spectroscopic line with the Lorentzian line shape, $\delta\nu_{HWHM}$ can be obtained, and is plotted as a function of P_p in Fig. 3f. From the intercept extracted by fitting the curve, we obtain the inhomogeneous dephasing time

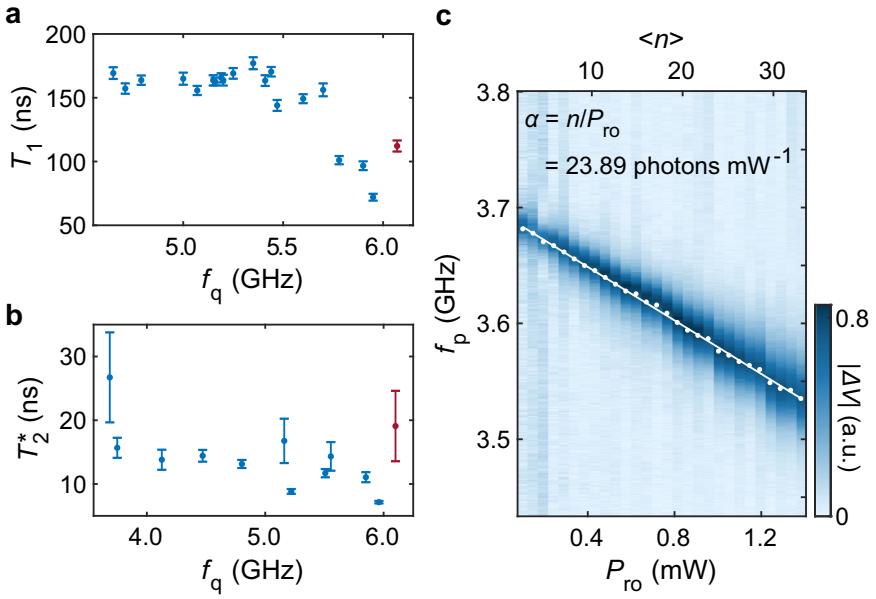

Fig. 4 The relaxation time T_1, inhomogeneous dephasing time T_2^*, and the ac Stark shift. a, **b** T_1 and T_2^* measured at different f_q, respectively (the data at $f_q = 6.07$ GHz shown in Fig. 3d, f are highlighted in red). Error bars represent the standard deviation. The measurements were carried out in the same way as shown in Fig. 3 (The experimental data and fitting process involved can be found in Supplementary Note 3). **c** Qubit spectrum as a function of the pump frequency f_p and the readout-generator power P_{ro} at $V_g = -1.1$ V. The pump-generator power is set to $P_p = 1$ mW and the resonator is probed on-resonance. The average photon number n in the resonator is converted from P_{ro} according to the ratio of the photon number to the readout power $\alpha = n/P_{ro} = 23.9$ photons mW^{-1}, shown in the upper abscissa. The qubit frequencies f_q (points) are extracted by the Lorentzian line shape fit to the spectrum, which is linearly fitted to the P_{ro} (line).

$T_2^* = 19.1 \pm 5.5$ ns $\ll 2T_1$ at $n \to 0$, indicating that the qubit dephasing is dominated by the pure dephasing time T_φ[39].

Gate voltage dependence of coherent times and the ac Stark effect

In order to distinguish the contributions of various noise sources to the qubit relaxation and decoherence, we repeated the T_1 and T_2^* measurement at different qubit frequencies by tuning the gate voltage. Figure 4a shows that the maximum of T_1 is ~180 ns, indicating that the qubit has relatively strong coupling with the TLSs and ambient noise. Possible solutions for eliminating the TLSs would include reducing the length of the junction region, using deep-etching trenches techniques, etc. As f_q gets closer to the resonator frequency f_r, T_1 drops from 180 to 70 ns. According to the formula $T_1 = [\pi D_{V,\perp}^2 S_V(f_q)]^{-1}$[39], where the $D_{V,\perp}$ is the transverse response coefficient of the qubit to the ambient voltage noise, $S_V(f_q)$ is the spectral density of the ambient voltage noise at qubit frequency, T_1 is mainly affected by high-frequency noise. Therefore, the drop in T_1 near f_r is caused by the enhanced coupling between the resonator and the qubit. Properly adjusting the coupling, and applying bandpass filters to the transmission line, might improve the qubit quality.

For the inhomogeneous dephasing time ($T_2^* \approx T_\varphi$), it is mainly sensitive to the low-frequency noise according to the formula $T_\varphi = [\pi D_{V,z}^2 S_V(0)]^{-1}$[39], where $D_{V,z}$ is the longitudinal response coefficient of the qubit to the ambient voltage noise and $S_V(0)$ is the spectral density of the low-frequency voltage noise. For gatemons, the low-frequency noise that affects the qubit is mainly introduced from the gate voltage circuit. Figure 4b shows that T_2^* in our experiment is about 15 ns on average. Its large fluctuation with f_q is presumably caused by the inaccuracy of this indirect way of determining T_2^*. There are several reasons for such a short dephasing time. Firstly, according to the ac Stark effect, the instability of the number of photons in the resonator can affect the dephasing time of the qubit[40]. Secondly, low-frequency noise such as the gate voltage noise affecting the energy difference of the qubit states also causes dephasing[41]. Improving the quality of the insulating layer in the bottom gate, such as using a high-quality single crystalline BN film as the insulating layer, or using a side gate configuration, could effectively reduce charge trapping and jumping in the gate, thereby avoiding the jumps in the qubit spectrum and also improving T_φ. In addition, T_φ can be improved by introducing on-chip low-pass filters to the gate line.

During weak continuous measurement, the qubit states are affected by photons in the cavity. Therefore, it is necessary to demonstrate that there are few photons in the resonator for the Rabi oscillation measurements. Figure 4c shows the response of the resonator spectrum with the power of the readout microwave signal P_{ro} to investigate the average photon number in the resonator. As the qubit is coupled with the resonator in the dispersive regime, there will be an ac Stark shift in the qubit frequency $f_q = f_{q0} + (2n+1)(g/2\pi)^2/(f_{q0} - f_r)$[37,38], where f_{q0} is the bare qubit frequency without coupling. The shift in the f_q is linearly related to the average number of photons n in the resonator, which is proportional to the power P_{ro}. By linearly fitting f_q to P_{ro}, the ratio of the photon number to the readout power $\alpha = n/P_{ro} = 23.9$ photons mW^{-1} can be obtained with the coupling strength $g/2\pi = 87$ MHz and the bare resonator frequency $f_r = 6.85$ GHz. The readout power P_{ro} adopted for the Rabi oscillation measurements in the time domain is 0.01 mW, and the corresponding average photon number n is about 0.24, well below 1, confirming that our measurements were in the weak measurement regime.

DISCUSSION

To summarize, we have successfully fabricated a Ge/Si nanowire-based hole-type superconducting gatemon qubit, and demonstrated the control of it in the frequency and time domains. The

tunable frequency spectrum, Rabi oscillation, energy relaxation time T_1 and inhomogeneous dephasing time T_2^* of the qubit were obtained, and the responses of T_1 and T_2^* with gate voltage were studied. Our results show that as the qubit-resonator coupling gradually increases, T_1 will be affected by environmental high-frequency noise introduced from the resonator, while T_2^*, which is mainly affected by low-frequency noise such as gating noise, has no obvious response to the coupling strength.

The coherence times of our device are comparable to the gatemons based on other materials in their early stages of development[32,42,43], and has the potential to be improved in the future. To reduce the trapped charges and the TLSs in the qubit, one can shorten the length of the JJ, and use a high-quality BN film as the insulating layer for the gate electrode. For improving the measurement system, one can add better filters to the transmission lines, to isolate the qubit from environmental noise.

Our Ge-based gatemon extends the superconducting qubit system from electrons to holes and on materials with strong spin-orbit coupling. In the future, it could be used to couple with the Andreev level qubits (ALQs) or Andreev spin qubits (ASQs) fabricated on the same Ge-based nanowires, mimicking what have been done on InAs nanowires[44,45]. The absence of hyperfine interaction in isotope-purified Ge/Si material would enable the ALQs and ASQs to have longer coherence time. Moreover, the strong and gate-tunable spin-orbit coupling in Ge/Si nanowires[11,46] would enable fast and all-electrical control of ASQs. Finally, since in hole-type semiconductor nanowires the Zeeman field required for hosting Majorana bound states (MBSs) is expected to be small[47], Ge/Si nanowire-based gatemons can hopefully survive in such a magnetic field, and thus are likely to support MBSs researches[1,47,48].

METHODS

The device fabrication proceeds in several steps described below. First, the sapphire substrate used in the chip is baked at 200 °C in a high vacuum environment to remove the organic impurities attached to it, and then a high-quality Al film with a thickness of 100 nm is deposited. Subsequently, the circuit elements are patterned by wet etching and the 3/10/3 nm thick Ti/Au/Ti bottom gate electrode is deposited by electronic beam evaporation. On top of the gate electrode, a 35 nm thick HfO_2 dielectric is grown by atomic layer deposition and then patterned by reactive ion etching. The Ge/Si nanowire is precisely placed on top of the dielectric using a nanowire transfer technique based on a tip and vitrified polypropylene carbonate. After placement, the Si shell around the nanowire was selectively removed by an argon milling step with electron beam lithography mask, and then Al electrodes with a thickness of 100 nm were deposited in situ. The Josephson junction with a length of about 30 nm is formed by the interdiffusion of Al and Ge after thermal annealing, which is performed in a vacuum probe station to enable real-time monitoring of the junction resistance. Finally, the Al electrodes of the junction are contacted to the capacitor island and to ground, respectively.

DATA AVAILABILITY

The data sets that support the findings of the present study will be available from the corresponding authors via email upon request.

CODE AVAILABILITY

All the custom code developed for this study will be available from the corresponding author via email upon request.

Received: 29 November 2022; Accepted: 15 May 2023;
Published online: 31 May 2023

REFERENCES

1. Scappucci, G. et al. The germanium quantum information route. *Nat. Rev. Mater.* **6**, 926–943 (2021).
2. Hanson, R. et al. Spins in few-electron quantum dots. *Rev. Mod. Phys.* **79**, 1217–1265 (2007).
3. Veldhorst, M. et al. An addressable quantum dot qubit with fault-tolerant control-fidelity. *Nat. Nanotechnol.* **9**, 981–985 (2014).
4. Hensen, B. et al. A silicon quantum-dot-coupled nuclear spin qubit. *Nat. Nanotechnol.* **15**, 13–17 (2020).
5. Barends, R. et al. Superconducting quantum circuits at the surface code threshold for fault tolerance. *Nature* **508**, 500–503 (2014).
6. Walter, T. et al. Rapid high-fidelity single-shot dispersive readout of superconducting qubits. *Phys. Rev. Appl.* **7**, 054020 (2017).
7. Kitaev, A. Y. Unpaired Majorana fermions in quantum wires. *Phys. Usp.* **44**, 131–136 (2001).
8. Dobbie, A. et al. Ultra-high hole mobility exceeding one million in a strained germanium quantum well. *Appl. Phys. Lett.* **101**, 172108 (2012).
9. Sammak, A. et al. Shallow and undoped germanium quantum wells: a playground for spin and hybrid quantum technology. *Adv. Funct. Mater.* **29**, 1807613 (2019).
10. Hao, X. J. et al. Strong and tunable spin-orbit coupling of one-dimensional holes in Ge/Si core/shell nanowires. *Nano Lett.* **10**, 2956–2960 (2010).
11. Kloeffel, C., Trif, M. & Loss, D. Strong spin-orbit interaction and helical hole states in Ge/Si nanowires. *Phys. Rev. B* **84**, 195314 (2011).
12. Yoneda, J. et al. A quantum-dot spin qubit with coherence limited by charge noise and fidelity higher than 99.9%. *Nat. Nanotechnol.* **13**, 102–106 (2018).
13. Hendrickx, N. W. et al. A single-hole spin qubit. *Nat. Commun.* **11**, 3478 (2020).
14. Hendrickx, N. W. et al. Fast two-qubit logic with holes in germanium. *Nature* **577**, 487–491 (2020).
15. Takeda, K. et al. Optimized electrical control of a Si/SiGe spin qubit in the presence of an induced frequency shift. *npj Quantum Inf.* **4**, 54 (2018).
16. Watzinger, H. et al. A germanium hole spin qubit. *Nat. Commun.* **9**, 3902 (2018).
17. Liu, H. et al. Gate-tunable spin-orbit coupling in a germanium hole double quantum dot. *Phys. Rev. Appl.* **17**, 044052 (2022).
18. Hu, Y., Kuemmeth, F., Lieber, C. M. & Marcus, C. M. Hole spin relaxation in Ge–Si core–shell nanowire qubits. *Nat. Nanotechnol.* **7**, 47–50 (2012).
19. Higginbotham, A. P. et al. Hole spin coherence in a Ge/Si heterostructure nanowire. *Nano Lett.* **14**, 3582–3586 (2014).
20. Froning, F. N. M. et al. Ultrafast hole spin qubit with gate-tunable spin–orbit switch functionality. *Nat. Nanotechnol.* **16**, 308–312 (2021).
21. Xiang, J. et al. Ge/Si nanowire mesoscopic Josephson junctions. *Nat. Nanotechnol.* **1**, 208–213 (2006).
22. de Vries, F. K. et al. Spin–orbit interaction and induced superconductivity in a one-dimensional hole gas. *Nano Lett.* **18**, 6483–6488 (2018).
23. Ridderbos, J. et al. Josephson effect in a few-hole quantum dot. *Adv. Mater.* **30**, 1802257 (2018).
24. Sistani, M. et al. Highly transparent contacts to the 1D hole gas in ultrascaled Ge/Si core/shell nanowires. *ACS Nano* **13**, 14145–14151 (2019).
25. Ridderbos, J. et al. Hard superconducting gap and diffusion-induced superconductors in Ge–Si nanowires. *Nano Lett.* **20**, 122–130 (2020).
26. Hendrickx, N. W. et al. Gate-controlled quantum dots and superconductivity in planar germanium. *Nat. Commun.* **9**, 2835 (2018).
27. Aggarwal, K. et al. Enhancement of proximity-induced superconductivity in a planar Ge hole gas. *Phys. Rev. Res.* **3**, L022005 (2021).
28. Tosato, A. et al. Hard superconducting gap in germanium. *Commun. Mater.* **4**, 23 (2023).
29. Vigneau, F. et al. Germanium quantum-well Josephson field-effect transistors and interferometers. *Nano Lett.* **19**, 1023–1027 (2019).
30. Hendrickx, N. W. et al. Ballistic supercurrent discretization and micrometer-long Josephson coupling in germanium. *Phys. Rev. B* **99**, 075435 (2019).
31. Conesa-Boj, S. et al. Boosting hole mobility in coherently strained [110]-oriented Ge–Si core–shell nanowires. *Nano Lett.* **17**, 2259–2264 (2017).
32. Larsen, T. W. et al. Semiconductor-nanowire-based superconducting qubit. *Phys. Rev. Lett.* **115**, 127001 (2015).
33. Koch, J. et al. Charge-insensitive qubit design derived from the Cooper pair box. *Phys. Rev. A* **76**, 042319 (2007).
34. Martinis, J. M. et al. Decoherence in Josephson qubits from dielectric loss. *Phys. Rev. Lett.* **95**, 210503 (2005).

35. Lisenfeld, J. et al. Electric field spectroscopy of material defects in transmon qubits. *npj Quantum Inf.* **5**, 105 (2019).
36. Wallraff, A. et al. Approaching unit visibility for control of a superconducting qubit with dispersive readout. *Phys. Rev. Lett.* **95**, 060501 (2005).
37. Schuster, D. I. et al. ac Stark shift and dephasing of a superconducting qubit strongly coupled to a cavity field. *Phys. Rev. Lett.* **94**, 123602 (2005).
38. Landig, A. J. et al. Coherent spin-photon coupling using a resonant exchange qubit. *Nature* **560**, 179–184 (2018).
39. Ithier, G. Manipulation, readout and analysis of the decoherence of a superconducting quantum bit. Université Pierre et Marie Curie - Paris VI (2005).
40. Schuster, D. I. et al. Resolving photon number states in a superconducting circuit. *Nature* **445**, 515–518 (2007).
41. Makhlin, Y. & Shnirman, A. Dephasing of qubits by transverse low-frequency noise. *JETP Lett.* **78**, 497–501 (2003).
42. Mergenthaler, M. et al. Circuit quantum electrodynamics with carbon-nanotube-based superconducting quantum circuits. *Phys. Rev. Appl.* **15**, 064050 (2021).
43. Wang, J. I. J. et al. Coherent control of a hybrid superconducting circuit made with graphene-based van der Waals heterostructures. *Nat. Nanotechnol.* **14**, 120–125 (2019).
44. Bargerbos, A. et al. Spectroscopy of spin-split Andreev levels in a quantum dot with superconducting leads. Preprint at https://arxiv.org/abs/2208.09314 (2022).
45. Pita-Vidal, M. et al. Direct manipulation of a superconducting spin qubit strongly coupled to a transmon qubit. *Nat. Phys.* (2023). https://doi.org/10.1038/s41567-023-02071-x.
46. Wang, R. et al. Electrical modulation of weak-antilocalization and spin–orbit interaction in dual gated Ge/Si core/shell nanowires. *Semicond. Sci. Technol.* **32**, 094002 (2017).
47. Mao, L. et al. Hole-doped semiconductor nanowire on top of an *s*-wave superconductor: a new and experimentally accessible system for Majorana fermions. *Phys. Rev. Lett.* **108**, 177001 (2012).
48. de Leon Nathalie, P. et al. Materials challenges and opportunities for quantum computing hardware. *Science* **372**, eabb2823 (2021).

ACKNOWLEDGEMENTS

This work was supported by the National Key Research and Development Program of China (Grant Nos. 2016YFA0300601, 2017YFA0304700 and 2015CB921402); by the National Natural Science Foundation of China (Grant Nos. 11527806, 92065203, 12074417, 11874406, 11774405 and 12174430); by the Strategic Priority Research Program B of the Chinese Academy of Sciences (Grants Nos. XDB33000000, DB28000000, and XDB07010100); by the Synergetic Extreme Condition User Facility (SECUF) which is sponsored by the National Development and Reform Commission; by the NSFC for Young Scholars (Grant No. E2J1141); by the Innovation Program for Quantum Science and Technology (Grant No. 2021ZD0302600); and by the Beijing Nova Program (Grant No. Z211100002121144).

AUTHOR CONTRIBUTIONS

E.Z., Z.L., X.Sun, and A.L. contributed equally to this work. A.L. and E.P.A.M.B. grew the Ge/Si core/shell nanowires. Z.L., E.Z., and X.Sun conceived and designed the experiment. E.Z., Z.L., X.Sun, and B.L. prepared the experimental set-up. E.Z. and Z.L. fabricated the qubit devices. E.Z., Z.L., and X.Sun conducted the measurements and analyzed the data. L.L., J.S., G.L., F.Q., X.Song, J.F., Z.J., and X.H. supported sample fabrication and measurements. E.Z. and Z.L. wrote the manuscript.

COMPETING INTERESTS

The authors declare no competing interests.

ADDITIONAL INFORMATION

Supplementary information The online version contains supplementary material available at https://doi.org/10.1038/s41534-023-00721-9.

Correspondence and requests for materials should be addressed to Zhaozheng Lyu or Li Lu.

Reprints and permission information is available at http://www.nature.com/reprints

Publisher's note Springer Nature remains neutral with regard to jurisdictional claims in published maps and institutional affiliations.